Electronic Supplementary Information

Directly Synthesis of 1T-phase MoS_2 Nanosheets with Abundance Sulfur-Vacancies through $(CH_3)_4N^+$ Cations-Intercalation for Hydrogen Evolution Reaction

Hongqiang Jin,[ab] Yu Yu,[c] Qikai Shen,[ab] Peipei Li,[ab] Jia Yu,[ab] Weiming Chen,[ab] Xin Wang,[d] Zhuo Kang,[d] Lei Zhu,[ab] Runqing Zhao,[ab] Lirong Zheng,*[e] Weiguo Song *[ab] and Changyan Cao *[ab]

[a] Beijing National Laboratory for Molecular Sciences, CAS Research/Education Center for Excellence in Molecular Sciences, CAS Key Laboratory of Molecular Nanostructure and Nanotechnology, Institute of Chemistry, Chinese Academy of Sciences, Beijing 100190, China

[b] University of the Chinese Academy of Sciences, Beijing 100049, China

[c] School of Science, Beijing Jiaotong University, Beijing 100044, China

[d] Beijing Advanced Innovation Center for Materials Genome Engineering, Beijing Key Laboratory for Advanced Energy Materials and Technologies and State Key Laboratory for Advanced Metals and Materials, School of Materials Science and Engineering, University of Science and Technology Beijing, Beijing 100083, China

[e] Beijing Synchrotron Radiation Facility (BSRF), Institute of High Energy Physics, Chinese Academy of Science, Beijing 100049, China.

*Correspondence: cycao@iccas.ac.cn; wsong@iccas.ac.cn; zhenglr@ihep.ac.cn

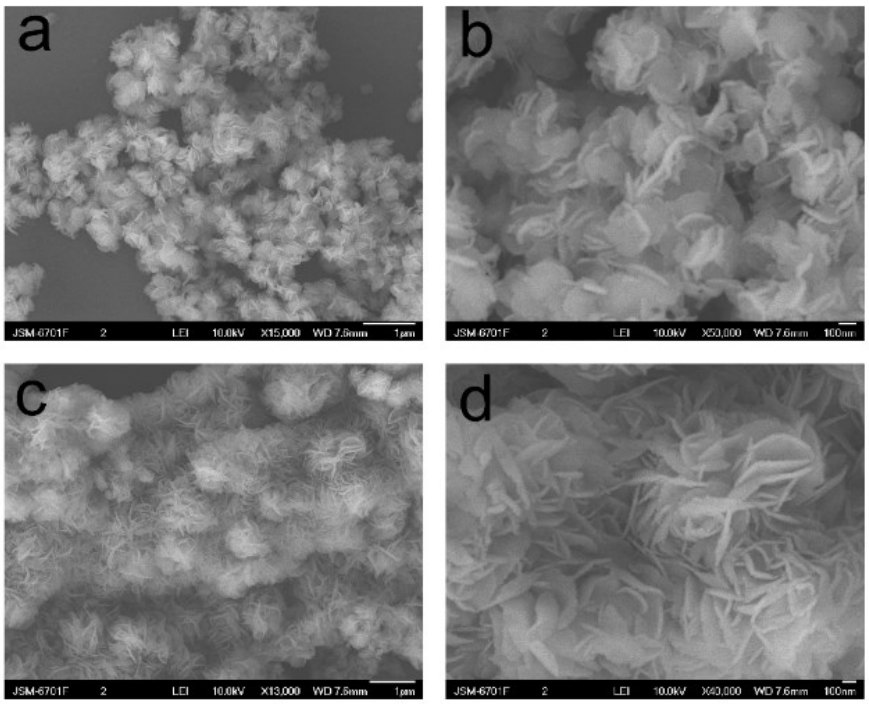

Fig.S1 SEM images of (a-b) bulk MoS_2 and (c-d) TMA-MoS_2.

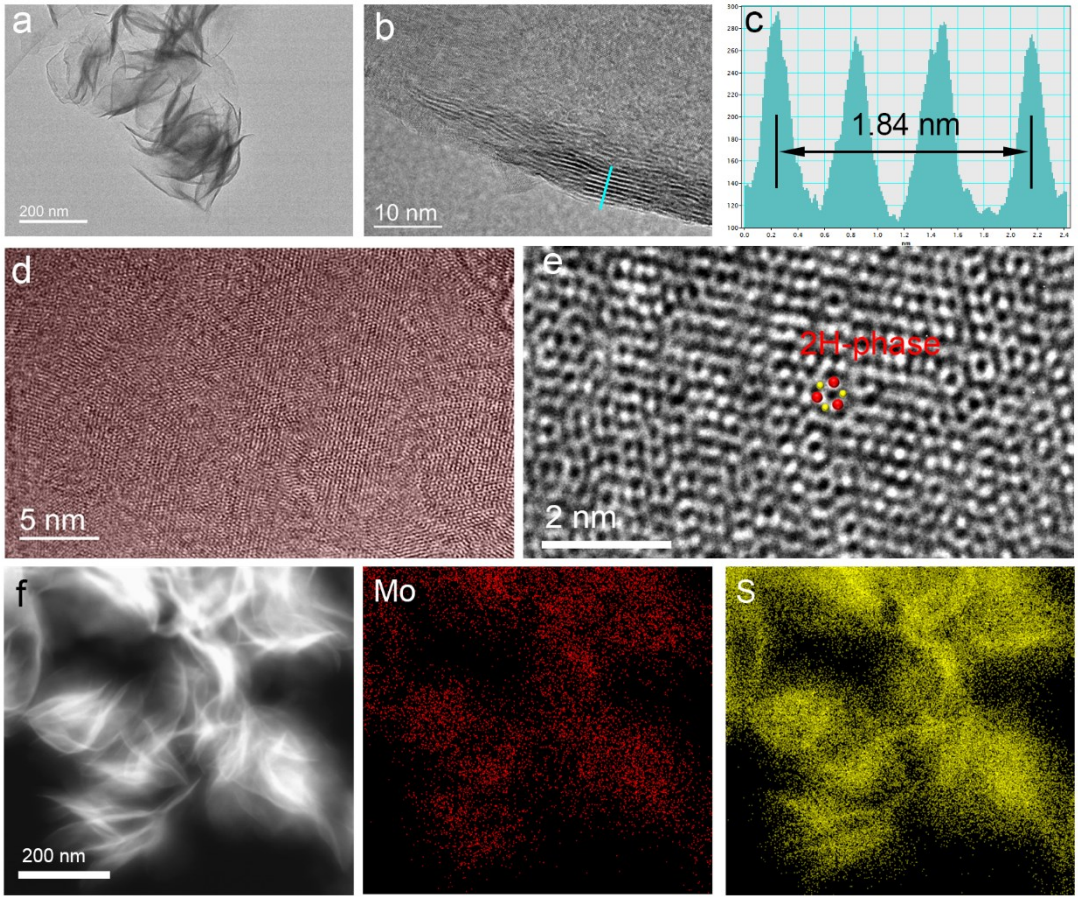

Fig.S2 (a-b) TEM and (c) the section profile along the blue line in (b) of bulk MoS_2. (d-e) HRTEM images and (f) HAADF-TEM with corresponding EDS elemental mapping images of bulk MoS_2. The average interlayer spacing is 6.13 Å consistent with XRD result, and the structure is mainly pure 2H-phase.

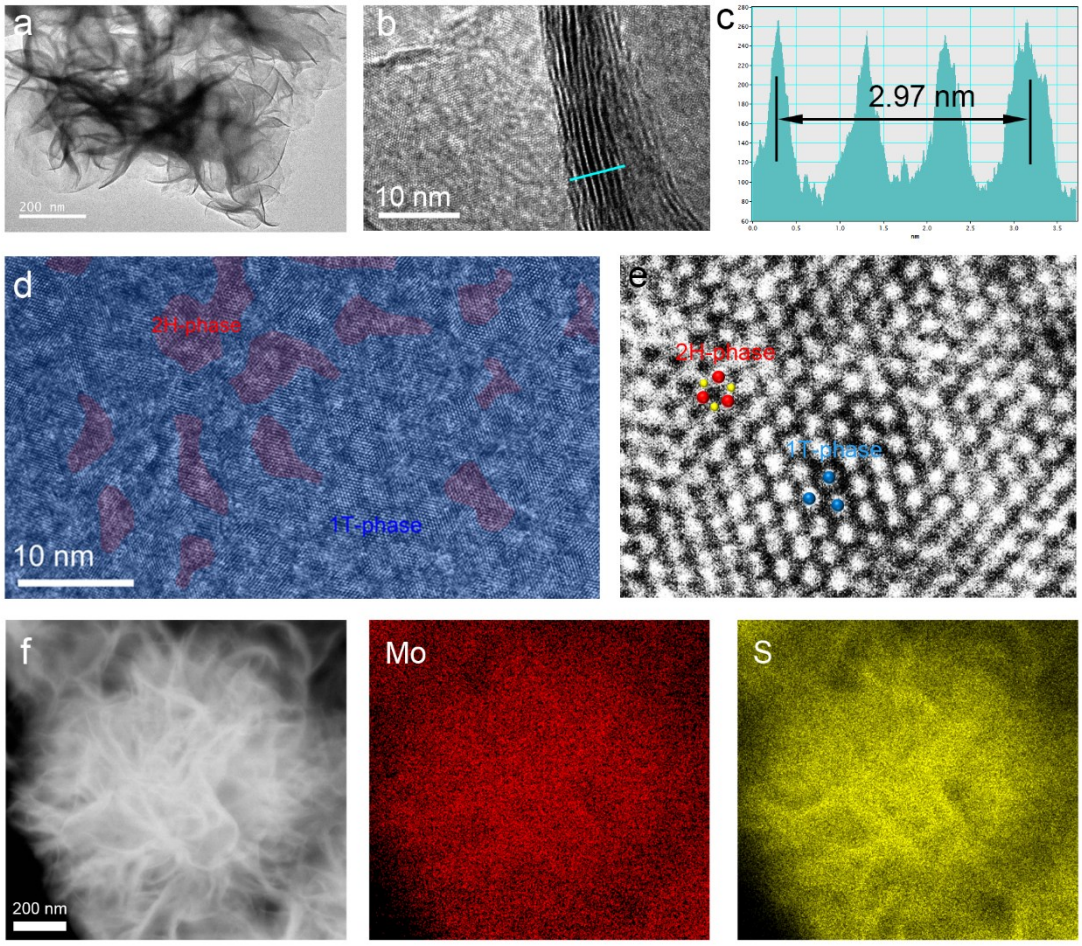

Fig.S3 (a-b) TEM and (c) the section profile along the blue line in (b) of TMA-MoS_2. (d-e) HRTEM images and (f) HAADF-TEM with corresponding EDS elemental mapping images of TMA-MoS_2. The average interlayer spacing of (002) plane is 9.9 Å, and the dominant structure is 1T-phase.

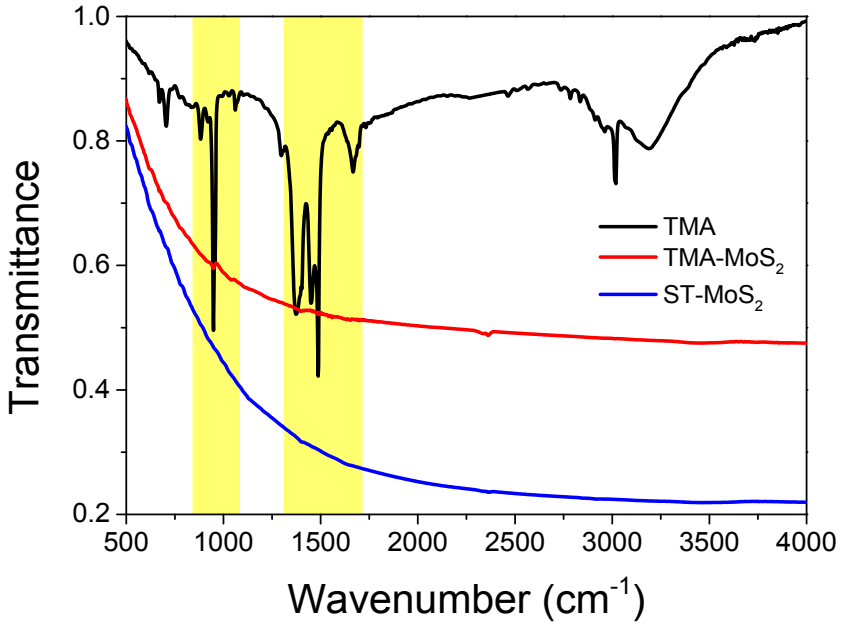

Fig.S4 Fourier transform infrared (FT-IR) spectra of TMA, TMA-MoS_2, and ST-MoS_2, suggesting the presence of TMA in the TMA-MoS_2 and absence of TMA in the ST-MoS_2 (the main range marked in yellow).

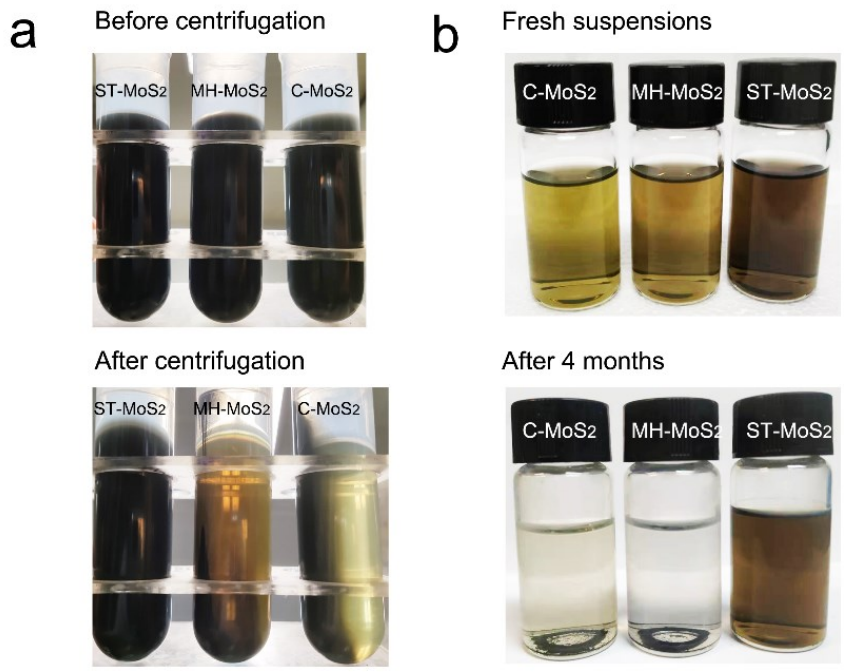

Fig.S5 (a) Optical images of C-MoS_2, MH-MoS_2, and ST-MoS_2 exfoliated from C-MoS_2, bulk MoS_2, and TMA-MoS_2 before and after centrifugation. The concentration of all samples is 1 mg/mL. (b) The colloidal photographs of C-MoS_2, MH-MoS_2, and ST-MoS_2 dispersed in 4:1 v/v IPA/H_2O solution and after 4 months. It clearly presents that the precipitation is not observed in the colloidal ST-MoS_2 solution even after 4 months. However, it is found in the C-MoS_2 and MH-MoS_2, respectively, suggesting that as-synthesized colloidal ST-MoS_2 nanosheets possess the best stability among the samples. This will be examined in the following zeta-potential measurement (**Fig. S9**).

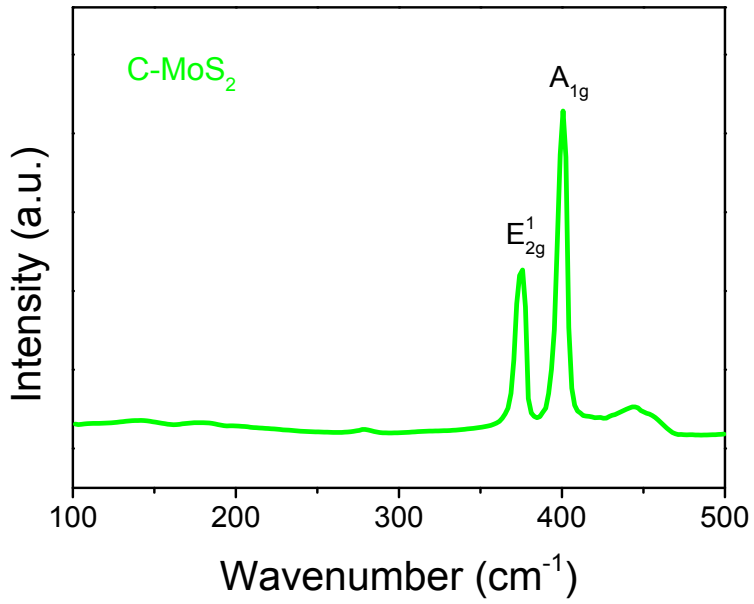

Fig.S6 Raman spectrum of C-MoS_2. Only two peaks at 380 and 406 cm^{-1} are observed, which corresponds to the in-plane vibration (E^{12}_g) and out-of-plane mode (A_{1g}), respectively, suggesting the 2H-phase structure.

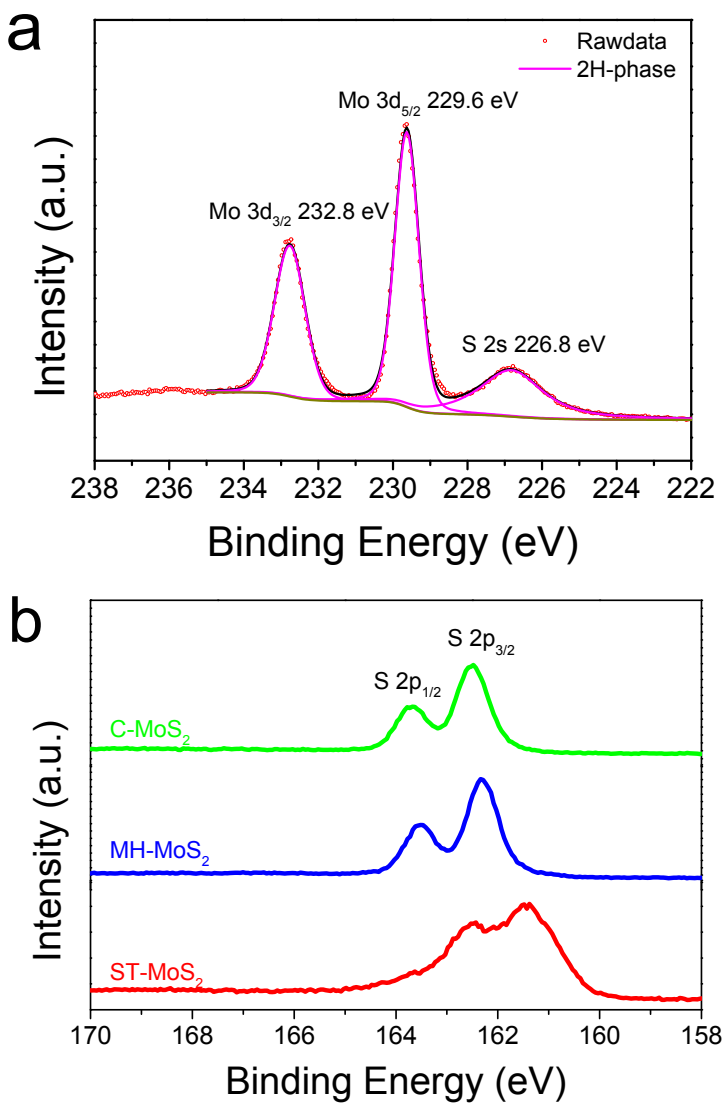

Fig.S7 (a) High-resolution XPS spectra of Mo 3d core-level peaks of C-MoS_2 and (b) S 2p core-level peaks of ST-MoS_2, MH-MoS_2 and C-MoS_2, respectively.

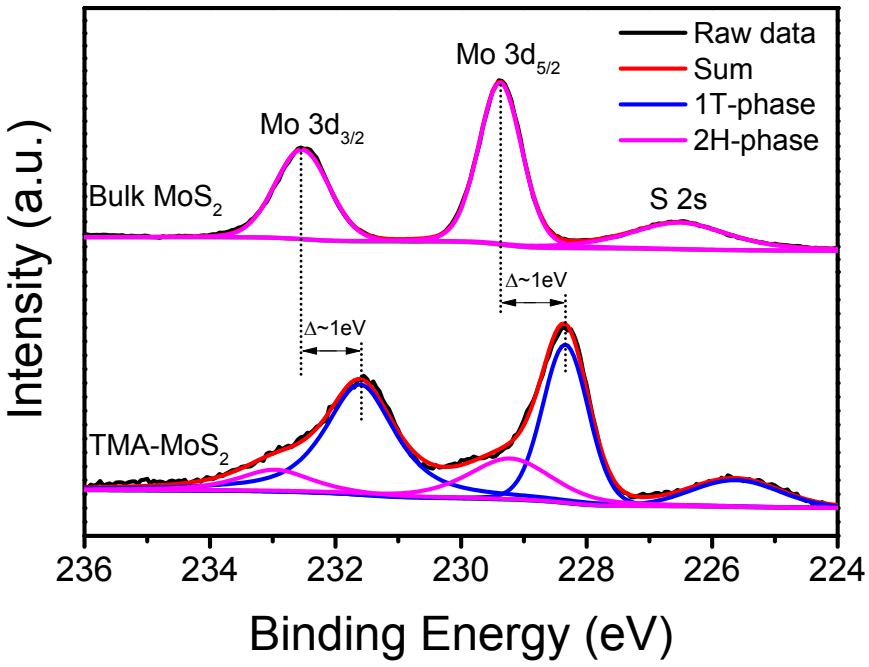

Fig.S8 High-resolution XPS spectra of Mo 3d core-level peaks of bulk MoS_2 and TMA-MoS_2. Both the Mo $3d_{3/2}$ and $3d_{5/2}$ peaks of TMA-MoS_2 were shifted to lower binding energies by about 1 eV with respect to those of bulk MoS_2 peaks, suggesting the 1T-pahse was formed during hydrothermal process rather than ultrasonic exfoliation.

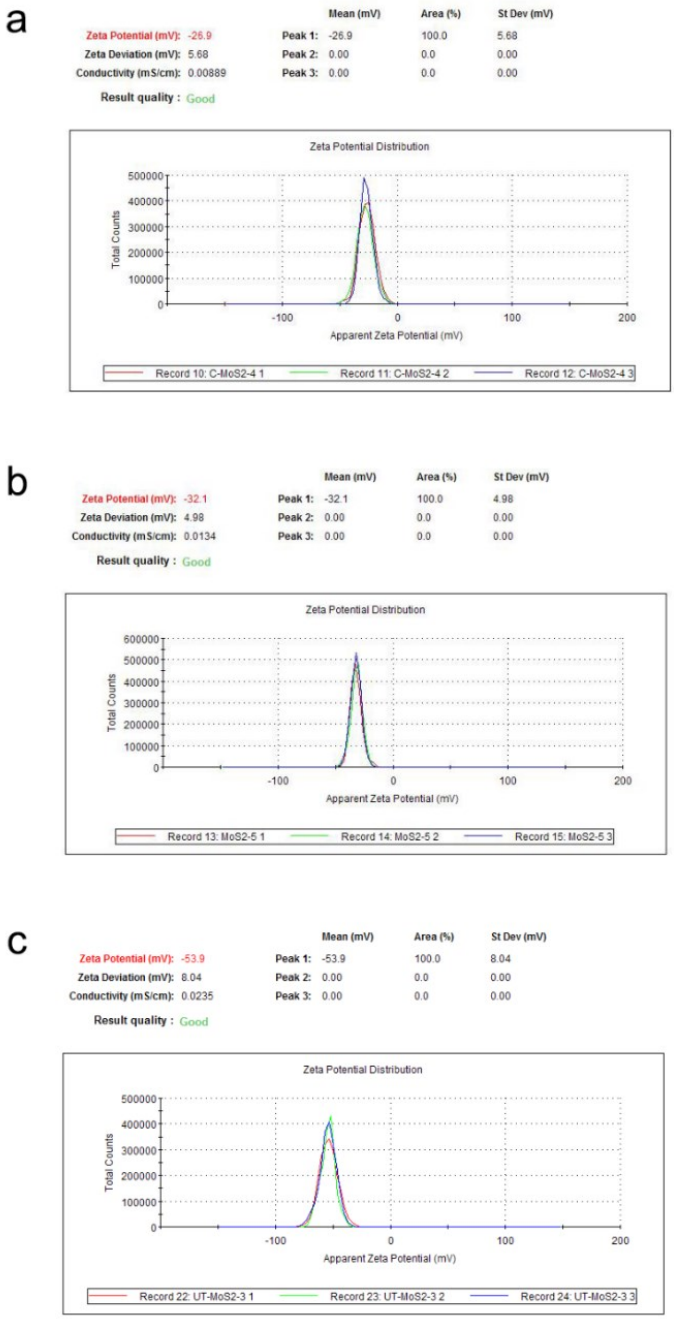

Fig.S9 Zeta-potential measurement of (a) C-MoS_2, (b) MH-MoS_2 and (c) ST-MoS_2 suspensions in 4:1 v/v IPA/H_2O solution with a concentration of 0.01 mg/mL. All samples are tested three times in parallel. Owing to the electrical double layers on the nanomaterial surface reflected to the nanomaterial solution stability, zeta-potential measurements were carried out. In general, good dispersed nanomaterials possess the zeta-potential values of less than -30 mV. [S16] Clearly, we can observe that the zeta-potential of MH-MoS_2 suspensions is -32.1 mV, indicating the as-synthesized MH-MoS_2 nanosheets possess a relative stability and negative charge surface. Notably, the zeta-potential of ST-MoS_2 (-53.9 mV) is more negative than that of C-MoS_2 and MH-MoS_2, suggesting the outstanding dispersed stability, which can be expected to the more exposed edges and basal planes of ST-MoS_2.

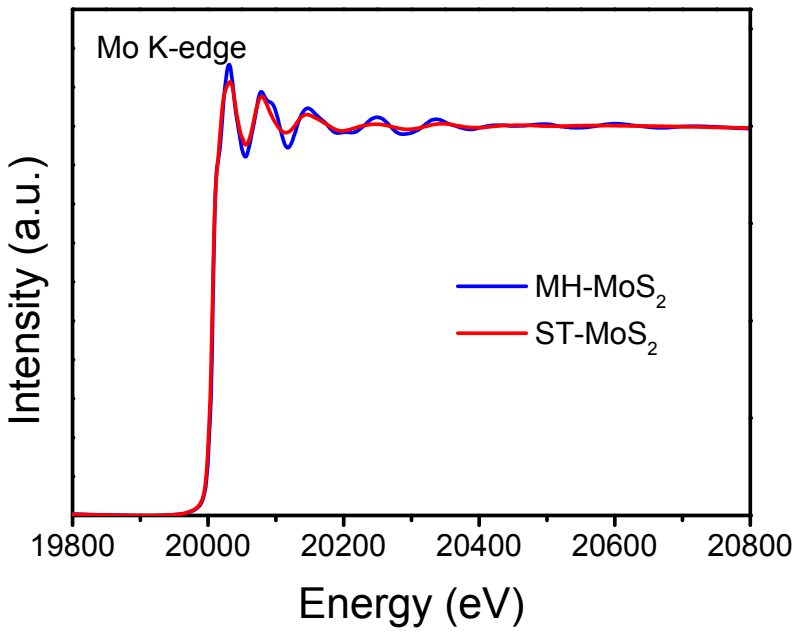

Fig.S10 The Mo K-edge X-ray absorption spectroscopy (XAS) spectra of MH-MoS_2 and ST-MoS_2.

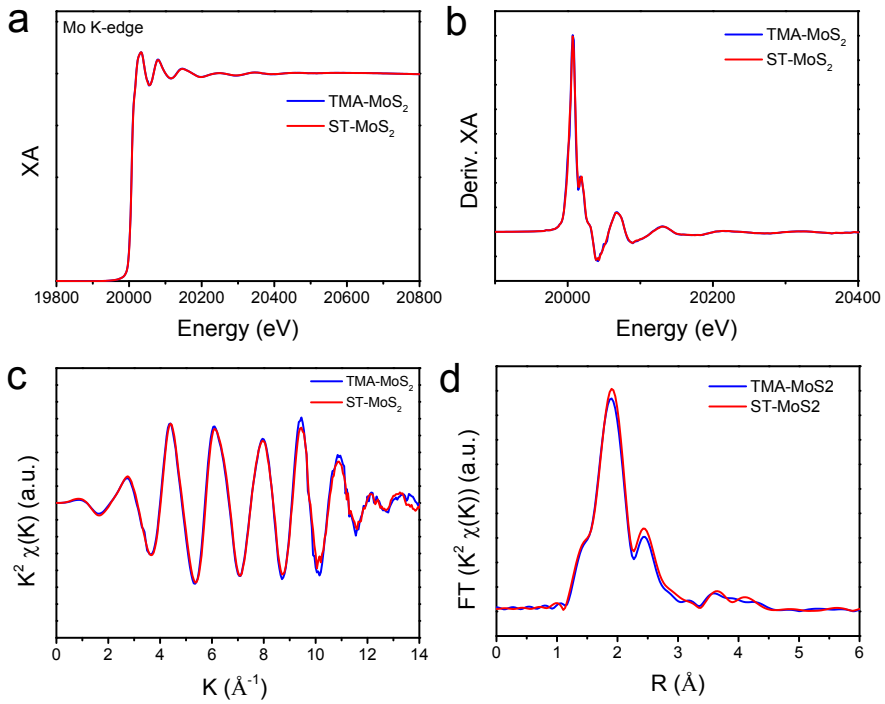

Fig.S11 (a) Mo K-edge XAS spectra and (b) derivative XAS spectra of ST-MoS_2 and TMA-MoS_2. (c) Mo K-edge EXAFS oscillations and (d) Fourier transform of the k^2-weighted Mo K-edge of the EXAFS spectra of ST-MoS_2 and TMA-MoS_2.

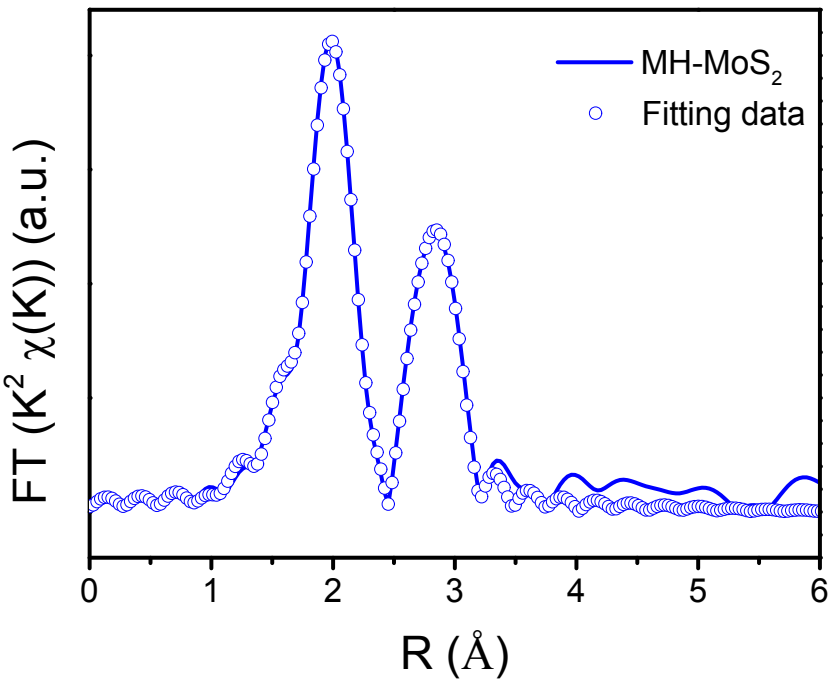

Fig.S12 The EXAFS fitting curves in R space of MH-MoS_2.

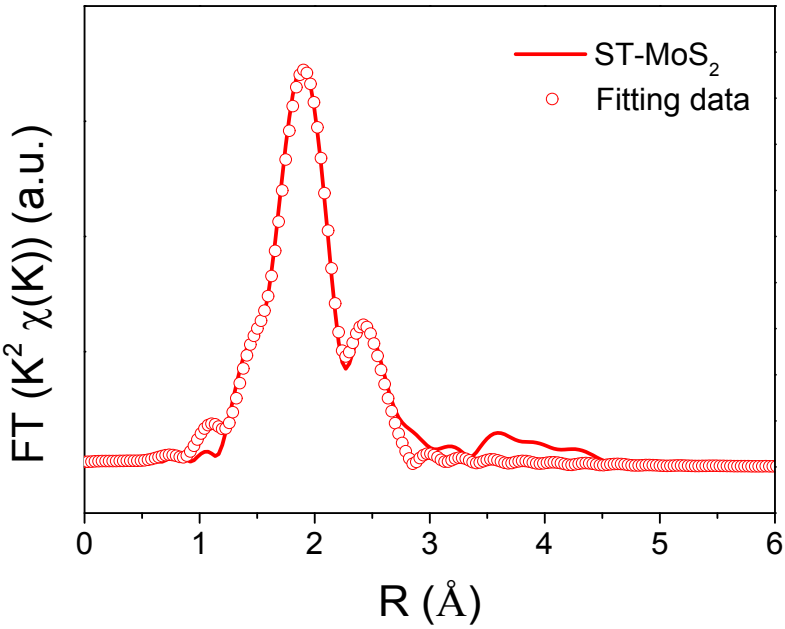

Fig.S13 The EXAFS fitting curves in R space of ST-MoS_2.

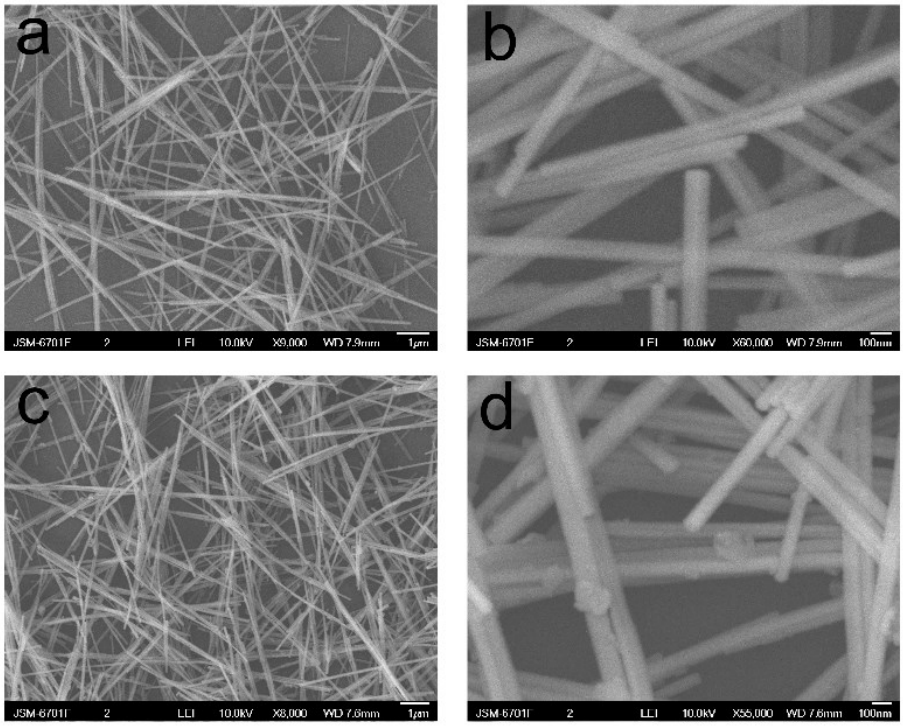

Fig.S14 SEM images of (a-b) pure CdS and (c-d) CdS/ST-MoS_2.

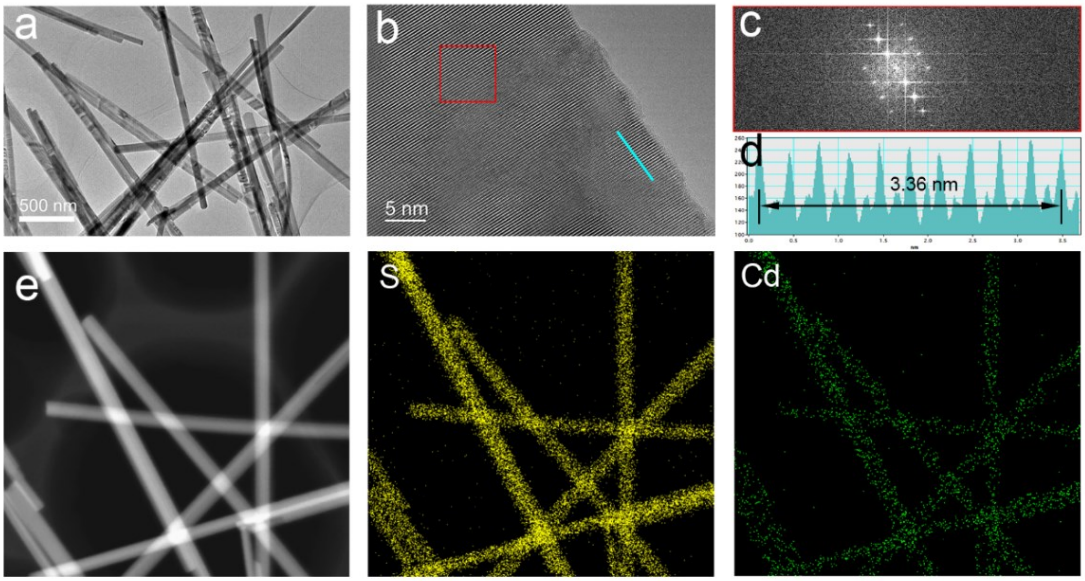

Fig.S15 (a) TEM, (b) HRTEM of pure CdS. (c) The corresponding FFT pattern marked with red square and (d) the section profile along the blue line in (b). (e) HAADF-TEM image with corresponding EDS elemental mapping images of pure CdS.

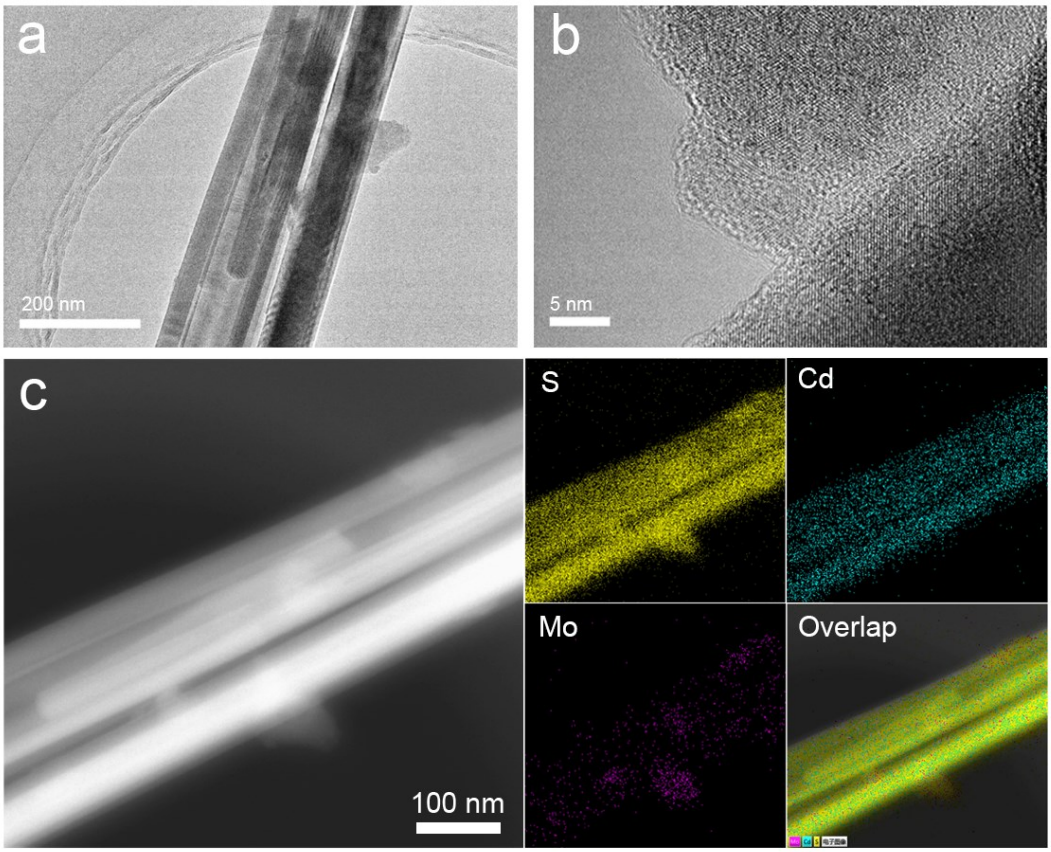

Fig.S16 (a) TEM, (b) HRTEM and (c) HAADF-TEM image with corresponding EDS elemental mapping images of CdS/ST-MoS_2.

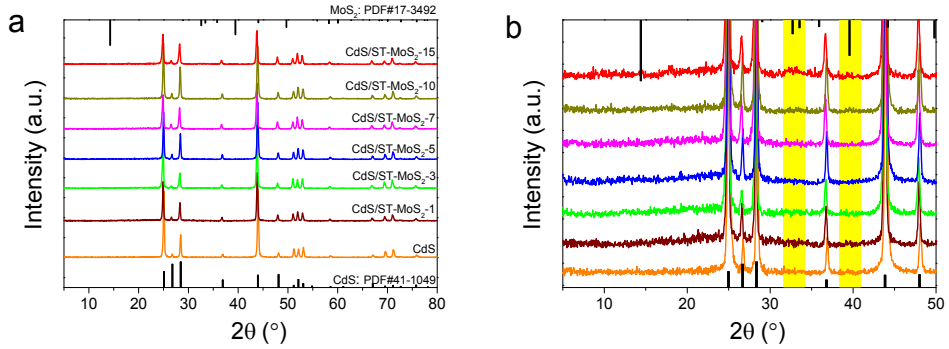

Fig.S17 XRD patterns of CdS and MoS_2/ ST-MoS_2 nanocomposites with varying MoS_2 loading. All the samples have similar diffraction peaks, which can be indexed to the hexagonal phase of CdS (PDF#41-1049). With the increase of the loading amount of ST-MoS_2, it can be observed that the weak diffraction peaks of ST-MoS_2, e.g., (100), (101), and (103) planes, gradually appear; this can be ascribed to the small amount or the low crystallization of ST-MoS_2.

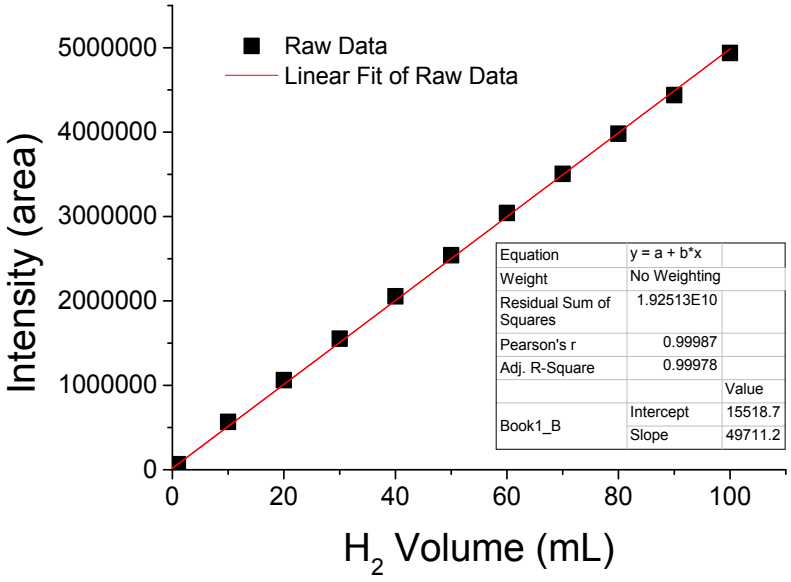

Fig.S18 Calibration curve collected with linear fit showing strong linear dependence of signal intensity to H_2 volume.

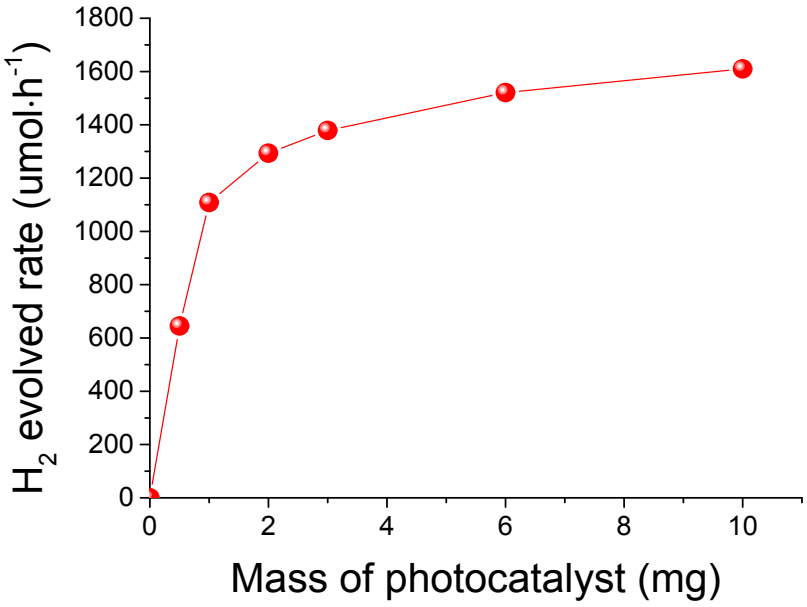

Fig.S19 The H_2 evolved rate changes along with the mass of CdS/ST-MoS_2. It is noted that the H_2 evolved rates don't linearly increase with respect to the photocatalyst mass due to the light-shielding effect. ref: 10.1016/j.joule.2021.01.001

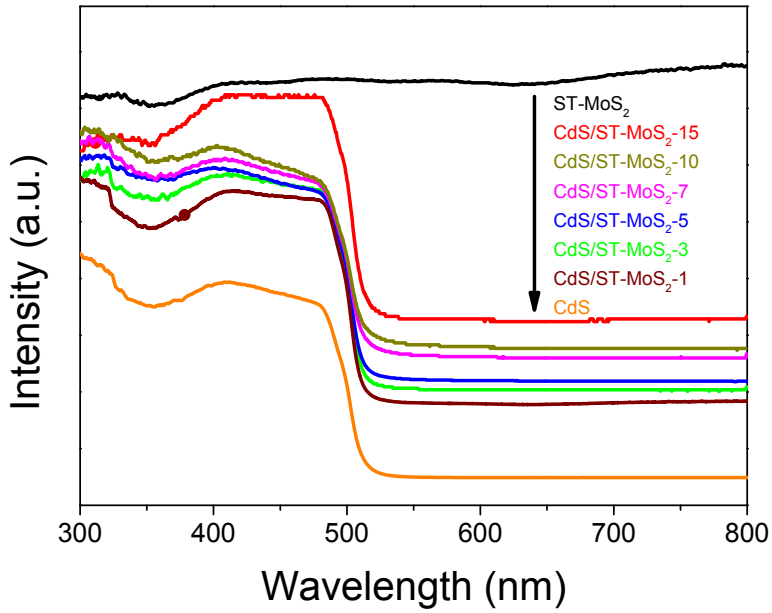

Fig.S20 UV/Vis diffuse reflectance spectra of CdS/ST-MoS_2 with various ST-MoS_2 loading. The pure CdS and CdS/ST-MoS_2-x samples appear a significant absorption at wavelength shorter than 520 nm, which is associated with the intrinsic bandgap absorption of the CdS semiconductor. Besides, it can be observed that the absorbance continuously increase, in visible light region from 520 to 800 nm, as the increase of the loading amount of UT-MoS_2. Although the adsorption of CdS/ST-MoS_2 is enhanced greatly when the loading amount of cocatalyst exceeds 7wt%, the HER performances exhibit a downward trend, which is ascribed to the "shielding effect".

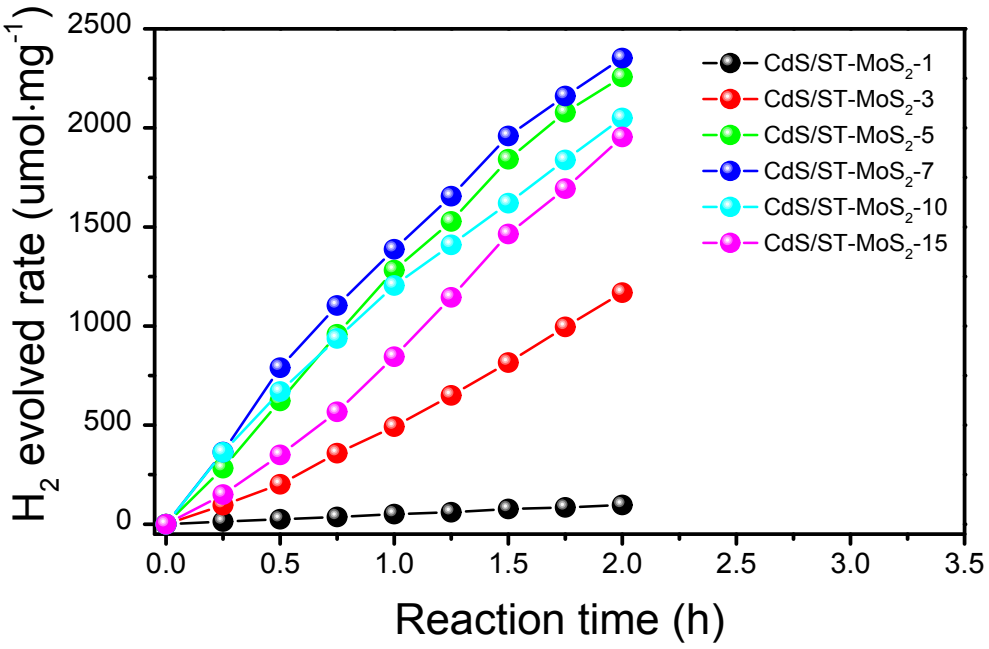

Fig.S21 The H_2 evolved rate changes along with the reaction time over various CdS/ST-MoS_2 photocatalysts.

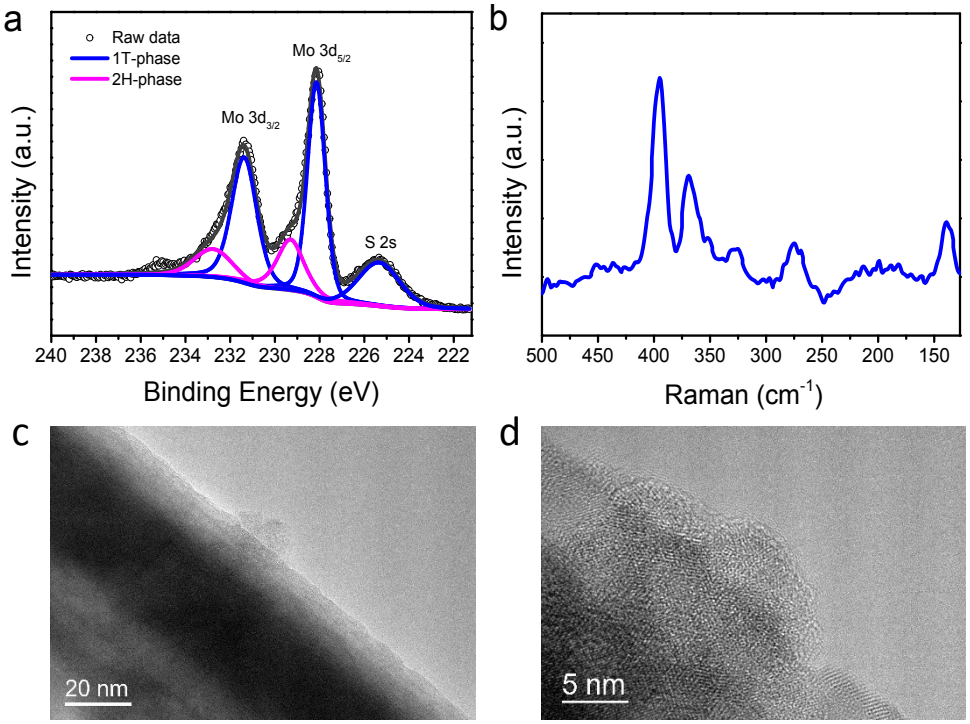

Fig.S22 (a) XPS, (b) Raman, (c) TEM, and (d) HRTEM images of the spent CdS/ST-MoS_2.

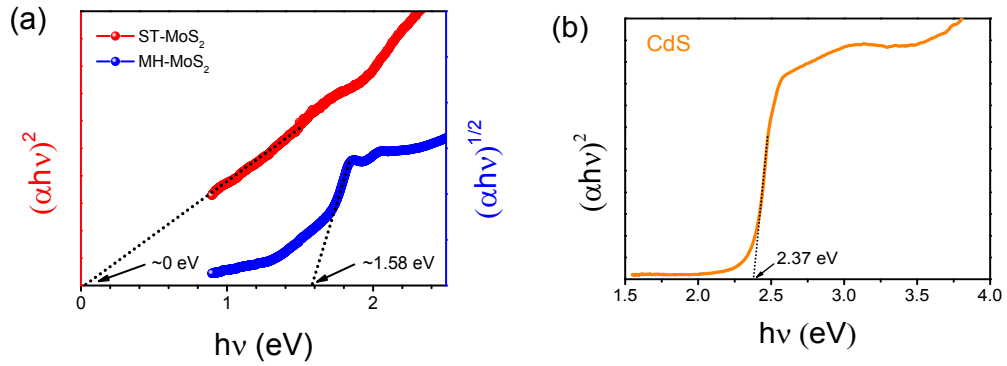

Fig.S23 Tauc plots ($(\alpha h\upsilon)^2$ vs. $h\upsilon$) converted form UV/Vis diffuse reflectance spectra of St-MoS_2, MH-MoS_2, and CdS.

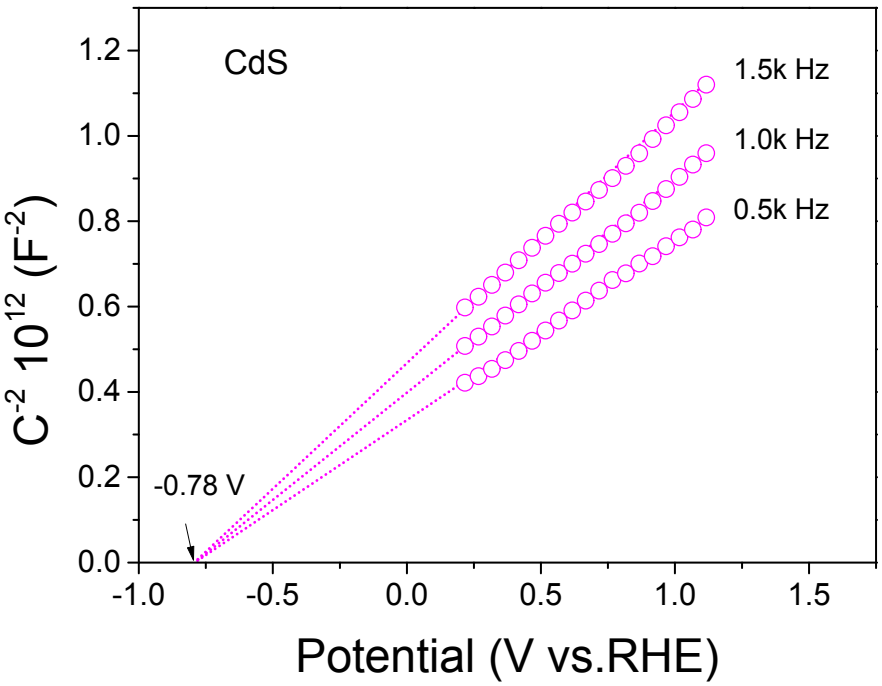

Fig.S24 Mott-Schottky plots of CdS collected at various frequencies.

Table S1. Elemental Analyses of ST-MoS_2.

Methods	Mo atom (%)	S atom (%)	S/Mo	S vacancies (%)
XPS	36.4	63.6	1.75	12.5
EDS	35.7	64.3	1.80	10.0

Table S2. The AQE values of various wavelength over CdS/ST-MoS_2.

Wavelength (nm)	420	450	500	550
Light intensity (mW)	125	137	162	148
Evolved H_2 (umol/h)	579	621	724	26.6
AQE (%)	73.4	67.0	59.4	2.2

For example, here we calculate the AQE value at 420 nm:

$$AQE = \frac{2 \times N_{H_2}}{\frac{I \times \lambda \times t}{h \times c}} \times 100\% = \frac{2 \times 6.02 \times 10^{23} \times 579 \times 10^{-6}}{\frac{125 \times 10^{-3} \times 420 \times 10^{-9} \times 3600}{6.61 \times 10^{-34} \times 3 \times 10^{8}}} \times 100\% = 73.4\%$$

Table S3. EXAFS fitting parameters at the Mo K-edge for various samples

Sample	Shell	N [a]	R (Å) [b]	σ^2 (Å^2·10^{-3}) [c]	ΔE0 (eV) [d]	*R* factor (%)
MH-MoS_2	Mo-S	5.8	2.41	3.2	3.4	**0.1**
	Mo-S-Mo	4.6	3.16	4.6	3.1	
ST-MoS_2	Mo-S	4.6	2.41	7.9	0.4	**0.8**
	Mo-Mo	1.2	2.76	7.5	1.5	
Standard MoS_2	Mo-S	6	2.41	2.9	2.1	**0.3**
	Mo-S-Mo	6	3.16	3.5	1.0	

[a] *N*: coordination numbers; [b] *R*: bond distance; [c] σ^2: Debye-Waller factors; [d] ΔE_0: the inner potential correction. *R* factor: goodness of fit. *S*02 were set as 0.965/0.965 for Mo-S/Mo-Mo, which was obtained from the experimental EXAFS fit of reference MoS_2 by fixing CN as the known crystallographic value and was fixed to all the samples.

Table S4. Comparison of HER performance in 0.5 M H_2SO_4 solution for 1T phase MoS_2-based electrocatalysts.

Samples	η(mV) at 10 mA/cm^2	Tafel slope (mV/dec)	References
ST-MoS_2	178	59	**This work**
MoS_2-8A	300	85	*ACS Nano 2019, **13**, 6824*
H_2O_2 treated MoS_2	131	48	*J. Am. Chem. Soc. 2020, **142**, 4298*
Co-1T MoS_2	195	46	*ACS Energy Lett.* 2018, ***3**,* 7
Ni-1T MoS_2	191	47	
1T- MoS_2	219	106	*Nat. Commun. 2019,* **10,** 982
FeO@1T- MoS_2	187	108	
CoO@1T- MoS_2	117	84	
Monolayer MoS_2	256	93	*J. Phys. Chem. Lett.* 2019*, **10**,* 4763
Ni-MoS2	>200	89	*J. Am. Chem. Soc.* 2017, ***139***, 15479
Metallic 1T MoS_2	175	41	*Nat. Commun.* 2016, ***7**,* 10672
1T- MoS_2	203	48	*J. Am. Chem. Soc. 2016, **138**, 7965*
MoS_2/Ni_3S_2	110	83	*Angew. Chem. 2016,* **55**, 6702
1T/2H- MoS_2	320	61	*ACS Appl. Mater. Inter. 2017, **9**, 25291*
T- MoS_2	290	78	*Nat. Energy 2017,* **2**, 17127

References

[S1] K. Chang, Z. Mei, T. Wang, Q. Kang, S. Ouyang, J. Ye, MoS2/Graphene Cocatalyst for Efficient Photocatalytic H-2 Evolution under Visible Light Irradiation, ACS Nano, 8 (2014) 7078-7087.

[S2] D. Lang, T. Shen, Q. Xiang, Roles of MoS2 and Graphene as Cocatalysts in the Enhanced Visible-Light Photocatalytic H-2 Production Activity of Multiarmed CdS Nanorods, Chemcatchem, 7 (2015) 943-951.

[S3] H. Huang, Z. Wang, B. Luo, P. Chen, T. Lin, M. Xiao, S. Wang, B. Dai, W. Wang, J. Kou, C. Lu, Z. Xu, L. Wang, Design of twin junction with solid solution interface for efficient photocatalytic H-2 production, Nano Energy, 69 (2020).

[S4] J. Wang, J. Luo, D. Liu, S. Chen, T. Peng, One-pot solvothermal synthesis of MoS2-modified Mn0.2Cd0.8S/MnS heterojunction photocatalysts for highly efficient visible-light-driven H-2 production, Applied Catalysis B-Environmental, 241 (2019) 130-140.

[S5] J. Jin, J. Yu, G. Liu, P.K. Wong, Single crystal CdS nanowires with high visible-light photocatalytic H-2-production performance, Journal of Materials Chemistry A, 1 (2013) 10927-10934.

[S6] N. Bao, L. Shen, T. Takata, K. Domen, Self-templated synthesis of nanoporous CdS nanostructures for highly efficient photocatalytic hydrogen production under visible, Chemistry of Materials, 20 (2008) 110-117.

[S7] G. Zhao, Y. Sun, W. Zhou, X. Wang, K. Chang, G. Liu, H. Liu, T. Kako, J. Ye, Superior Photocatalytic H-2 Production with Cocatalytic Co/Ni Species Anchored on Sulfide Semiconductor, Advanced Materials, 29 (2017).

[S8] T. Simon, N. Bouchonville, M.J. Berr, A. Vaneski, A. Adrovic, D. Volbers, R. Wyrwich, M. Doeblinger, A.S. Susha, A.L. Rogach, F. Jackel, J.K. Stolarczyk, J. Feldmann, Redox shuttle mechanism enhances photocatalytic H-2 generation on Ni-decorated CdS nanorods, Nature Materials, 13 (2014) 1013-1018.

[S9] K. Zhang, J.K. Kim, B. Park, S. Qia, B. Ji, X. Sheng, H. Zeng, H. Shin, S.H. Oh, J.H. Park, C.-L. Lee, Defect-Induced Epitaxial Growth for Efficient Solar Hydrogen Production, Nano Letters, 17 (2017) 6676-6683.

[S10] L. Yin, X. Hai, K. Chang, F. Ichihara, J. Ye, Synergetic Exfoliation and Lateral Size Engineering of MoS2 for Enhanced Photocatalytic Hydrogen Generation, Small, 14 (2018).

[S11] K. Chang, X. Hai, H. Pang, H. Zhang, L. Shi, G. Liu, H. Liu, G. Zhao, M. Li, J. Ye, Targeted Synthesis of 2H-and 1T-Phase MoS2 Monolayers for Catalytic Hydrogen Evolution, Advanced Materials, 28 (2016) 10033-10041.

[S12] X.-L. Yin, G.-Y. He, B. Sun, W.-J. Jiang, D.-J. Xue, A.-D. Xia, L.-J. Wan, J.-S. Hu, Rational design and electron transfer kinetics of MoS2/CdS nanodots-on-nanorods for efficient visible-light-driven hydrogen generation, Nano Energy, 28 (2016) 319-329.

[S13] X.-H. Zhang, N. Li, J. Wu, Y.-Z. Zheng, X. Tao, Defect-rich O-incorporated 1T-MoS2 nanosheets for remarkably enhanced visible-light photocatalytic H-2 evolution over CdS: The impact of enriched defects, Applied Catalysis B-Environmental, 229 (2018) 227-236.

[S14] D.A. Reddy, H. Park, R. Ma, D.P. Kumar, M. Lim, T.K. Kim, Heterostructured WS2-MoS2 Ultrathin Nanosheets Integrated on CdS Nanorods to Promote Charge Separation and Migration and Improve Solar-Driven Photocatalytic Hydrogen Evolution, Chemsuschem, 10 (2017) 1563-1570.

[S15] D.P. Kumar, S. Hong, D.A. Reddy, T.K. Kim, Noble metal-free ultrathin MoS2 nanosheet-

decorated CdS nanorods as an efficient photocatalyst for spectacular hydrogen evolution under solar light irradiation, Journal of Materials Chemistry A, 4 (2016) 18551-18558.
[S16] D.A. Reddy, H. Park, S. Hong, D.P. Kumar, T.K. Kim, Hydrazine-assisted formation of ultrathin MoS2 nanosheets for enhancing their co-catalytic activity in photocatalytic hydrogen evolution, Journal of Materials Chemistry A, 5 (2017) 6981-6991.
[S17] M. Gopannagari, D.P. Kumar, D.A. Reddy, S. Hong, M.I. Song, T.K. Kim, In situ preparation of few-layered WS2 nanosheets and exfoliation into bilayers on CdS nanorods for ultrafast charge carrier migrations toward enhanced photocatalytic hydrogen production, Journal of Catalysis, 351 (2017) 153-160.
[S18] J. He, L. Chen, Z.-Q. Yi, C.-T. Au, S.-F. Yin, CdS Nanorods Coupled with WS2 Nanosheets for Enhanced Photocatalytic Hydrogen Evolution Activity, Industrial & Engineering Chemistry Research, 55 (2016) 8327-8333.
[S19] Y. Chen, Z. Qin, General applicability of nanocrystalline Ni2P as a noble-metal-free cocatalyst to boost photocatalytic hydrogen generation, Catalysis Science & Technology, 6 (2016) 8212-8221.
[S20] J. Choi, D.A. Reddy, N.S. Han, S. Jeong, S. Hong, D.P. Kumar, J.K. Song, T.K. Kim, Modulation of charge carrier pathways in CdS nanospheres by integrating MoS2 and Ni2P for improved migration and separation toward enhanced photocatalytic hydrogen evolution, Catalysis Science & Technology, 7 (2017) 641-649.
[S21] S. Cao, Y. Chen, C.-J. Wang, X.-J. Lv, W.-F. Fu, Spectacular photocatalytic hydrogen evolution using metal-phosphide/CdS hybrid catalysts under sunlight irradiation, Chemical Communications, 51 (2015) 8708-8711.
[S22] Z. Sun, H. Zheng, J. Li, P. Du, Extraordinarily efficient photocatalytic hydrogen evolution in water using semiconductor nanorods integrated with crystalline Ni2P cocatalysts, Energy & Environmental Science, 8 (2015) 2668-2676.
[S23] X. Zhang, H. Liang, H. Li, Y. Xia, X. Zhu, L. Peng, W. Zhang, L. Liu, T. Zhao, C. Wang, Z. Zhao, C.-T. Hung, M.M. Zagho, A.A. Elzatahry, W. Li, D. Zhao, Sequential Chemistry Toward Core-Shell Structured Metal Sulfides as Stable and Highly Efficient Visible-Light Photocatalysts, Angewandte Chemie-International Edition, 59 (2020) 3287-3293.
[S24] J. Wang, B. Li, J. Chen, N. Li, J. Zheng, J. Zhao, Z. Zhu, Enhanced photocatalytic H-2-production activity of CdxZn1-xS nanocrystals by surface loading MS (M = Ni, Co, Cu) species, Applied Surface Science, 259 (2012) 118-123.
[S25] H. Du, K. Liang, C.-Z. Yuan, H.-L. Guo, X. Zhou, Y.-F. Jiang, A.-W. Xu, Bare Cd1-xZnxS ZB/WZ Heterophase Nanojunctions for Visible Light Photocatalytic Hydrogen Production with High Efficiency, Acs Applied Materials & Interfaces, 8 (2016) 24550-24558.
[S26] S.R. Lingampalli, U.K. Gautam, C.N.R. Rao, Highly efficient photocatalytic hydrogen generation by solution-processed ZnO/Pt/CdS, ZnO/Pt/Cd1-xZnxS and ZnO/Pt/CdS1-xSex hybrid nanostructures, Energy & Environmental Science, 6 (2013) 3589-3594.
[S27] X. Hai, K. Chang, H. Pang, M. Li, P. Li, H. Liu, L. Shi, J. Ye, Engineering the Edges of MoS2 (WS2) Crystals for Direct Exfoliation into Monolayers in Polar Micromolecular Solvents, Journal of the American Chemical Society, 138 (2016) 14962-14969.